Comparison of three types of XPAD3.2 / CdTe single chip hybrids for hard X-ray applications in material science and biomedical imaging

C. Buton[a,*], A. Dawiec[a], J. Graber-Bolis[b], K. Arnaud[b], J. F. Bérar[c], N. Blanc[c], N. Boudet[c], J. C. Clémens[b], F. Debarbieux[b], P. Delpierre[d], B. Dinkespiler[d], T. Gastaldi[b], S. Hustache[a], C. Morel[b], P. Pangaud[b], H. Perez-Ponce[d], E. Vigeolas[b]

[a] *Synchrotron SOLEIL, L´Orme des Merisiers, Saint-Aubin — BP 48 91192, GIF-sur-YVETTE CEDEX, France*
[b] *CPPM, Aix-Marseille Université, CNRS/IN2P3, Marseille, France*
[c] *Université Grenoble Alpes, Institut NÉEL, F-38042 Grenoble, France – CNRS , Institut NÉEL, F-38042 Grenoble, France*
[d] *im*XPAD *SAS — Espace Mistral, Athélia IV, 297 avenue du Mistral, 13600 La Ciotat, France*

Abstract

The CHIPSPECT consortium aims at building a large multi-modules CdTe based photon counting detector for hard X-ray applications. For this purpose, we tested nine XPAD3.2 single chip hybrids in various configurations (*i.e.* Ohmic *vs.* Schottky contacts or electrons *vs.* holes collection mode) in order to select the most performing and best suited configuration for our experimental requirements. Measurements have been done using both X-ray synchrotron beams and ^{241}Am source. Preliminary results on the image quality, calibration, stability, homogeneity and linearity of the different types of detectors are presented.

Keywords: X-ray detectors, Hybrid pixel detectors

1. Introduction

Modern X-ray imaging systems allow to obtain images immediately after exposure. The systems based on amorphous silicon photo-diodes and CCD detectors are very commonly used. Two decades ago, new types of X-ray imagers based on photon counting instead of charge integration during exposure have been introduced for particle tracking in high energy physics experiments [1]. This approach called quantum X-ray imaging is capable of discriminating and processing each single X-ray photon in addition to counting them. It also offers improved image quality and noise subtraction compared to the former devices [2] while operating at room temperature. In this so-called *hybrid* approach where analytic electronic chain is physically bound to each pixel, the sensor material can be chosen according to the energy of the X-ray photons to be detected and its electronics custom-designed for specific applications [3, 4]. Sensor and electronics are assembled using bump-bonding and flip-chip technologies resulting in a hybrid-pixels photon counting detector.

Silicon based hybrids are now regularly used in X-ray detectors for material science and for the development of photon counting and spectral micro-computed tomography (CT) [5, 6, 7, 8, 9, 10, 11]. However, the detective quantum efficiency of thin (500 microns) silicon based hybrids is decreasing steadily from 90% at 12 keV to less than 40% at 20 keV [8, 9]. Therefore, a grown interest in studying new high-density and high-Z sensor materials for X-ray imaging at energies above 25 keV appeared (*i.e.* for third generation synchrotron sources or new generation of medical X-ray detectors). Thanks to its high resistivity at room temperature and its large linear attenuation coefficient, the cadmium-telluride (CdTe) appeared to be a good prospective material for room temperature semiconductor detectors.

This paper reports tests that have been performed both with radioactive sources and on synchrotron beamlines. We will determine the best suited configuration for the production of hybrids with CdTe sensors using either Schottky or Ohmic contacts in hole or electron collection modes, bump bonded to the different flavors of the XPAD3.2 chip. Several single chip hybrids were assembled and evaluated, allowing for the selection of the detector type. Their linearity, stability robustness were evaluated in order to chose the most relevant technology for building a large detector composed of 56 single chip modules dedicated to material science and preclinical imaging.

2. Hybrid pixels detectors

2.1. The cadmium telluride sensors

The CdTe semiconductor sensor material has a higher Z than Si and a higher density, and thus a better X-ray absorption efficiency. Nevertheless, despite the recent progress in growing and processing this material, good quality and homogeneous sensors are not yet available in sizes comparable to silicon. Furthermore, they are fragile and the bump bonding process needs to be optimized.

Cadmium telluride is a II-VI semiconductor. A couple of methods are currently available to grow CdTe crystals: the *traveling heater method* (THM) used by Acrorad[1] in Japan, for the

*Corresponding author
Email address: clement.buton@synchrotron-soleil.fr (C. Buton)

[1] http://www.acrorad.co.jp/us

Table 1: CdTe sensor main physical characteristics at 300 K [12]

Band gap [eV]	e^-/h^+ energy [eV]	Density $[g \cdot cm^{-3}]$	Intrinsic resistivity $[\Omega \cdot cm^{-3}]$	e^- mobility $[cm^2 \cdot V^{-1} \cdot s^{-1}]$	h^+ mobility $[cm^2 \cdot V^{-1} \cdot s^{-1}]$	e^- lifetime [s]	h^+ lifetime [s]
1.4	4.4	6.2	$\simeq 10^9$	1000	80	10^{-4}	10^{-4}

fabrication of CdTe substrates and the *high pressure Bridgman* (HPB) used by eV-products[2] in the USA to produce CdZnTe substrates.

For the tests described in this paper, we have selected 9 high-resistivity Acrorad 500 μm thick CdTe sensors (p-types operated either in hole collection mode or in electron collection mode). We have already successfully used such sensors in a previous study and they gave us satisfactory results [3]. The main physical characteristics of the material are presented in Table 1.

2.2. Metallic contacts — Ohmic & Schottky

In order to become real sensors, semiconductor crystals need to be equipped with electrodes. This is done by depositing metallic contacts on the substrate surfaces. Depending on the setup, the sensors can work either in hole collection mode or in electron collection mode, with positive or negative input charges to the pixel. Two distinct types of CdTe sensors have been fabricated by Acrorad: "Ohmic" and "Schottky". Whereas Ohmic circuits are reported to be stable over time, the Schottky ones offer better energy resolution and higher detection count rates.

Ohmic sensors have Pt contacts on both surfaces [13]. The charge collection mode depends on the applied bias polarity, and can be chosen at the expense of a higher reverse current for the h^+ mode (for example, ~ 2 μA at -200 V).

Because Schottky contacts are blocking ones they allow for reduction of the bias reverse current by at least one order of magnitude which seems more suitable for most applications. They are obtained by depositing (In/Ti) weld either on the pixel side (electron collection) or on the entrance side (hole collection), while setting a Ohmic Pt contact on the opposite side.

This type of detectors exhibits a well known polarization effect [14, 15], which leads to a progressive decrease of the amplitude of pulses due to charge trapping. This effect can however be compensated by periodic sensor polarization resets [3]. It is also worth noting that in CdTe, holes mobility is an order of magnitude lower than for electrons (*cf.* Table 1). This fact is *a priori* in favor of e^- rather than hole collection, either with Ohmic or Schottky contacts.

The characteristics and performances of 3 types of CdTe sensors bump bonded to XPAD3 chips were studied in more details: Ohmic detectors used in electrons collection mode and Schottky detectors used both in electrons and holes collection mode (*cf.* Table 2). Ohmic sensors working in holes collection mode were discarded from the study due to the presence of very high leakage currents.

[2] http://www.evproducts.com

2.3. The read-out chips

The XPAD3 read-out chip has already been extensively discussed elsewhere [16, 3, 17] and therefore we have been describing only its main features in this section (*cf.* Table 3). The XPAD3.2 chip is designed in sub-micron, radiation hard IBM 0.25 μm technology. It comprises 9600 square pixels of 130 μm^2 organized in 120 rows $\times$ 80 columns.

This chip has been designed in 2 different versions, which differ mainly by their input charge polarity: the first one (XPAD3.2-S) expects positive charges at its input, whereas the second (XPAD3.2-C) expects negative ones. Therefore, the Schottky sensors in holes collection mode have been hybridized on XPAD3.2-S chips while Schottky circuits in electrons collection mode and Ohmic circuits have been hybridized on XPAD3.2-C chips.

Table 3: XPAD3.2 chip main characteristics. Note that the energy needed to create an electron-hole pair is 3.64 eV in Si and 4.44 eV in CdTe. These values were obtained with the global register parameters "IMFP" and "ITUNE" set to 25 and 110, respectively (*cf.* [17] for a description of the global registers). For instance, setting the thresholds at 50 keV requires to increase the threshold step value.

Version	XPAD3.2-S	XPAD3.2-C
Number of pixels	9600	
Pixel size	130 μm $\times$ 130 μm	
Read-out time	1 ms / frame	
Counter depth	12 bits + overflow	
Counting rate	10^6 photons / pixel / s	
Power consumption	40 μW / pixel	
Selectivity mode	1 threshold	
Gain	23 nA / 100 e^-	18 nA / 100 e^-
Gain (CdTe)	52 nA / keV	41 nA / keV
Nonlinearity	10% at 17700 e^-	10% at 19500 e^-
Global electronic noise	100 e^- rms	
Threshold step	135 e^- rms	110 e^- rms
Threshold dispersion	75 e^- rms	60 e^- rms

The circuit for each pixel is composed of a two-stages analogue part (charge detection and selection) followed by a 12-bit counter with an overflow bit (*cf.* Figure 1). The counter increments by one unit for each photon detected with an energy higher than the threshold value previously selected by the user. The energy threshold for each individual pixel is the result of a global adjustment for the whole chip and a local in-pixel digital-to-analogue converter (DAC) tuning to compensate for local variability of the pixels.

Each XPAD3.2 chip is equipped with a "spy pixel" that has buffered analogue outputs from the preamplifier and transconductance amplifier (OTA). This means that the inspection of

Table 2: Denomination of all hybrids provided by Acrorad together with the detector configurations and characteristics used during the different test campaigns.

circuit	name	board	dead pixels [#]	used at SOLEIL	used at CPPM	used at ESRF	comments
Ohmic e^-	1-1	DE2	801	×	√	×	/
Ohmic e^-	1-3	C4	2	√	×	×	Unconnected bumps
Ohmic e^-	1-4	C4	40	×	√	×	/
Schottky h^+	2-1	DE2	/	×	×	×	Most pixels are dead
Schottky h^+	2-4	C4	6	×	√	×	/
Schottky h^+	2-5	C4	3	√	×	√	A few less efficient pixels
Schottky e^-	3-2	C4	83	√	×	×	Heterogeneous counting
Schottky e^-	3-4	C4	18	×	×	√	/
Schottky e^-	3-5	DE2	48	×	√	×	Two dead zones

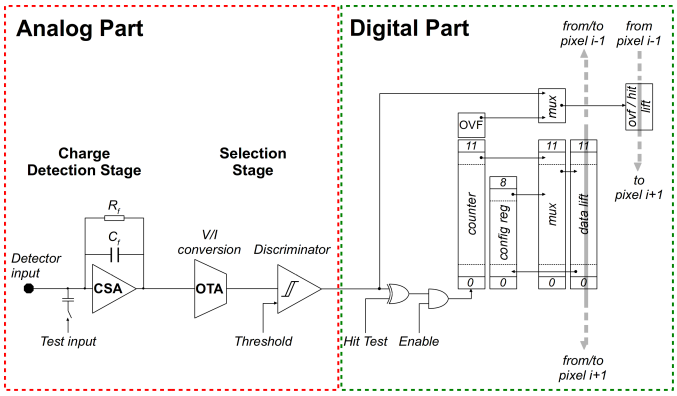

Figure 1: Pixel design schematic displaying both stages of the analog part as well as the digital part [17].

analogue signals at each stage of amplification is possible, which has been proven to be very useful for high voltage selections (*cf.* §5.1).

2.4. Hybridization

The separation between readout electronics and sensor enables an independent optimization of each part. Both elements of the detector are connected together in the final stage of the production using the bump-bonding (indium bumps in the case of silicon sensors on XPAD) and flip-chip technologies.

The hybridization of CdTe crystal to read-out electronics is more problematic than for silicon sensors. Temperature and metal etchants are harmful for CdTe surface, leading usually to a dramatic reduction of inter-pixel resistance [3]. The Finnish microelectronics company Ajat[3] has developed a low-temperature Sn/Bi solder process including CdTe surface protection by aluminium nitride passivation film that has been employed in our case.

2.5. The evaluation boards

Nine hybrids have been produced and wire-bonded to conventional printed circuit "mono" boards for evaluation purpose. In order to avoid any damage to the very fragile contacts, sensor bias was done by a single wire touching the contact.

Two different readout systems were used during the tests. The "DE2" evaluation board was aimed at developing, testing and evaluating the first XPAD3.1 chips. It offers a lot of testing possibilities, one of them being the access to the output of the "spy pixel". However, it is not an acquisition board and its software is not made for routine measurements on synchrotron beam lines for example. For this specific purpose, we used the commercial "C4" board from imXPAD[4] together with their proprietary software. As connectors between "DE2" and "C4" cards are not compatible, the small "mono" boards dedicated for single detector were developed in two different versions.

Three USB boxes with processing boards have been provided by imXPAD to mount the detectors (see pictures 2).

3. Calibration

To ensure that each individual pixel of the matrix is sensitive to the same energy range, the discriminator threshold of the pixel counting chain has to be calibrated. As mentioned in §2.3, there are two different thresholds, one global per chip and one local per pixel. The global threshold of the matrix is adjusted by setting the "ITH" current. However, due to variability in the microelectronic processes, the natural distribution of the actual energy threshold for a given ITH value is pretty large across the pixels of the matrix. A fine and local tuning of the pixels is thus required. That is the reason why a local 6-bit DAC (DACL) has been implemented in each pixel.

Due to the fact that the signal amplitude value is lost after discrimination, the threshold has to be derived from the digital output of the chip. We have thus used a method based on the injection of a given number of charge impulses of known amplitude to the analog front-end electronics. The response of the discriminator can then be studied when varying the threshold settings. As a result, a curve representing the pixel's count versus its threshold can be determined. This curve has a characteristic "S" shape with a counting "plateau" and the method

[3] http://www.ajat.fi

[4] http://www.imxpad.com

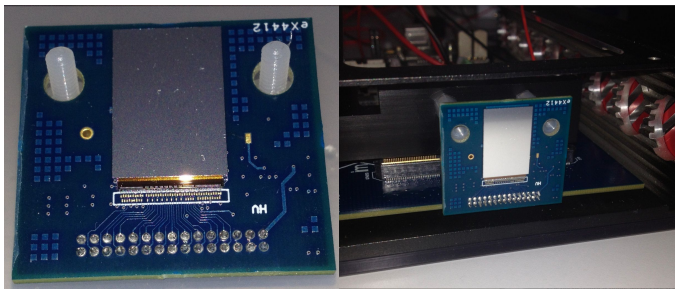

(a) Chip on acquisition "mono" board (b) Board mounted in the USB box

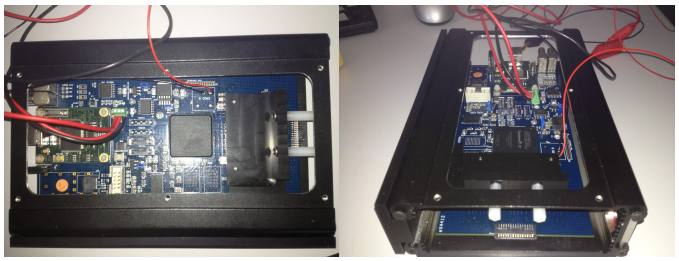

(c) USB box (top view) (d) USB box (front view)

Figure 2: Pictures of one of the USB box provided by imXPAD with an XPAD3.2 detector mounted on its acquisition "mono" card.

of calibration is then called the "S-curve" method. The generic acquisition procedure for the calibration of a single chip can be summarized as follows:

- Setting of all the pixel DACL values to their average value (*i.e.* DACL = 32 in our case).
- Determination of the global threshold value (ITH): step by step decrement of the global threshold from its highest value (*i.e.* where almost no pixels are counting) until the value where half of the pixels are counting. The chip's global threshold is then set to this particular value.
- Acquisition of the images corresponding to the increment of the DACL value (*i.e.* from 0 to 63) on every pixel.

This results in a single data cube (of dimension 120×80 pixels $\times$ 64 DACL) containing 9600 "S-curves" representing the count rates measured as a function of the DACL value for each pixel.

The fine calibration process consists in finding the best DACL value for each pixel from its "S-curve" derived from a DACL scan. Several methods are available to achieve this goal, but we will focus here only on an *ad hoc* method (see § 3.2). A comparative and thorough analysis of different calibration methods is currently in preparation and will be presented in [18].

Hybrid pixel detectors are affected by charge sharing between neighbouring pixels [19, 20], especially when pixels are small. This non-negligible effect influences not only the spatial resolution and the measured energy spectrum, but also the detector count rate. Hybrid pixel detectors require a monochromatic beam of known energy to be properly calibrated. In order to decrease the charge sharing effect the calibration should be set at half the working energy. It allows to discriminate between pulses of a given photon on neighbouring pixels and select only the one above the threshold, thus counting the photon only once.

3.1. *Over-the-noise*

The simplest possibility to select the DACL value is to set the pixel's threshold just above the electronic noise (*i.e.* at the lowest practicable threshold) without using any external physical signal. This "over-the-noise" method, quick and easy to implement, ensures that the threshold will be in the counting regime but does not give the best results due notably to the bad management of the charge sharing effect.

3.2. *At a given energy*

Calibration of the thresholds at a given energy is obtained by setting each DACL value as close as possible to the abscissa of the inflection point of the "S-curve" resulting from the irradiation of the detector by a flat field monochromatic beam of this energy.

To achieve this goal, we developed a numerical *ad hoc* method that focuses only on the data, without any other biases. In a concern of efficiency, we used the python[5] array[6] abilities so as to find the thresholds in all the "S-curves" of the data cube at the same time, which improves greatly the speed and robustness of the algorithm. The major advantage of this *ad hoc* method is its robustness and reliability. It can be trained on different data sets and fine tuned accordingly. It is especially efficient for the "non-typical" pixels, since the degrees of freedom are under strong constraints. Admittedly, this method benefits greatly from the discrete configuration of the DACs and would be much less accurate if the DACL steps were narrower.

The calibration process result is a threshold map of the detector. An example of this map for the Schottky h^+ [2-5] configuration at 16 keV can be seen of Figure 3.

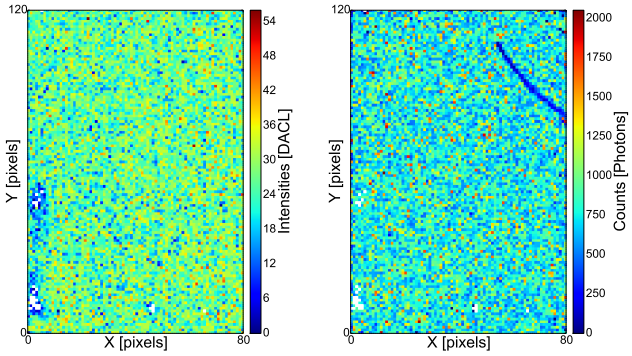

Figure 3: Threshold map (left) and count map at threshold (right) for the Schottky h^+ [2-5] configuration at 16 keV. The high voltage wire as well as the pixels edge effects are easily noticeable on the count map. Zones that have been damaged during manipulations are clearly visible on the lower left side of the threshold map.

[5] http://www.python.org
[6] http://www.numpy.org

4. Setup & dataset

Measurements have been carried out on the beamlines D2AM[7] and *Métrologie*[8] of the third generation light sources ESRF[9] and SOLEIL, respectively. Intensive tests have also been performed in the laboratory at CPPM[10] using an Americium (^{241}Am) source (59.6 keV γ-rays).

To prepare these experiments, we came across some supply difficulties due to the fragility of the sensors (as already discussed in §2.1). In particular our first batch of hybrids was broken into pieces due to overheating during the transfer of the chips on the printed circuit board. This waste of time had some consequences on the fulfillment of the tests and on the scheduling of the experiments on the synchrotron beamlines. For these reasons, we finally decided to test at least once each hybrid. Thus, even though we could not compare directly the results, we would be able to have an overview of the different detectors characteristics.

The second batch of detectors (*i.e.* the nine tested in this article) arrived just in time for the test campaign at SOLEIL. We therefore had to run our tests without optimization of the high voltage, which was achieved later at CPPM.

4.1. Experimental setups

For both measurement campaigns at ESRF and SOLEIL, the experience setups were similar and very simple (a scheme of the installation is shown in fig 4). In order to get a field of view as homogeneous and flat as possible we used a scatterer (either air, Teflon or glass) right after the beam entrance. Then, the hybrid pixel detector was placed one meter downstream, slightly shifted in order to avoid direct beam illumination, but close enough to get a sufficient amount of photons.

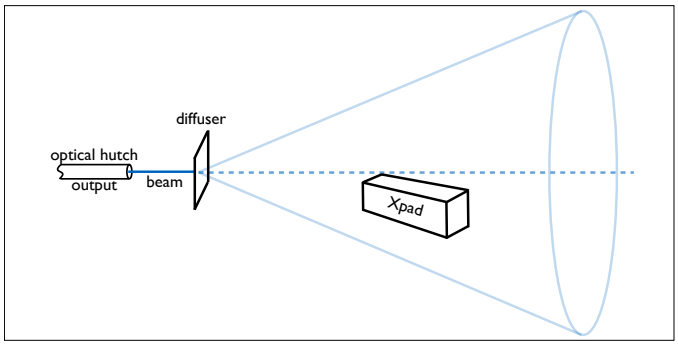

Figure 4: Schematic of the beamline setup for basic calibration / test measurements with an XPAD detector. On the D2AM beamline, we used some layer of Teflon as scatterer, whereas on the *Métrologie* beamline we used either glass or just air depending on the energy of the beam. The detector is slightly shifted to avoid direct beam illumination.

[7] http://www.esrf.eu/UsersAndScience/Experiments/CRG/BM02

[8] http://www.synchrotron-soleil.fr/Recherche/LignesLumiere/METROLOGIE

[9] European Synchrotron Radiation Facility

[10] *Centre de Physique des Particules de Marseille*

4.2. Data sample

During our measurements campaign at SOLEIL, we essentially focused on testing the calibration process for several energies and on assessing the quality of the resulting images at 24 keV. Only 3 out of 6 sensors (one of each kind) available on C4 boards were tested (*cf.* §2). For each detector configuration, we performed DACL scans at eight different energies (the characteristics of the measurements performed at SOLEIL are summarized on Table 4). Each scan was then used to produce calibration maps thanks to the *ad hoc* method (*cf.* §3.2). Note that, at energies above 16 keV, three microscope glass slides (3×1 mm) were used to scatter the beam.

Table 4: Details of the calibration measurements undertaken at SOLEIL (*cf.* §5.2 and Figure 6).

(a) Energies in chronological order of measurements

Beam energies [keV]							
8	12	16	32	40	24	27	13.5

(b) Non optimized biases

Biases [V]		
Ohmic e^- [1-3]	Schottky e^- [3-2]	Schottky h^+ [2-5]
−100	−400	+400

At CPPM, tests have been performed using the americium source on the spy pixel of three different chips in order to optimize their bias value. Note that, being unable to calibrate at half energy with an americium source, the detectors were calibrated using the "over-the-noise" method for these tests. The second part of this test campaign aimed at studying the counting stability with time of three detector configurations by taking successive images interspersed with bias resets (the corresponding measurement characteristics are summarized on Table 5).

Table 5: Details of the conditions used to assess the stability measurements undertaken at CPPM with an ^{241}Am source (*cf.* §5.3 and Figure 9).

detector type	exposure time [s]	reset cycle [min]	exposure number [#]	bias [V]
Ohmic e^- [1-3]	150	×	240	−200
Schottky e^- [3-5]	40	20	460	−400
Schottky h^+ [2-4]	40	10	400	+900

Then the followup measurements campaign at ESRF aimed at assessing the counting stability on a beamline using the bias settings that have been optimized at CPPM. For each of the three selected detectors, a DACL scan has been performed at 12 keV. The resulting scans allowed to produce a calibration map thanks to the *ad hoc* method. Then, the beam energy was moved to 24 keV (or twice the calibration energy). At this energy, 3.5 cm of water were necessary to scatter the light and obtain a reasonably flat field. When correctly calibrated, we

proceeded to the counting stability measurements by imposing different bias reset cycles during the acquisitions (*cf.* Table 6 for a summary of the measurement characteristics).

Table 6: Details of the conditions used to assess the stability and leakage current measurements at 24 keV undertaken at ESRF with different bias reset cycles (*cf.* §5.3 and Figure 10). Due to lack of time, and since the Ohmic type does not need resets, the tests on the Ohmic chip have not been performed.

detector type	exposure time [s]	reset cycle [min]	exposure number [#]	bias [V]
Schottky e^- [3-4]	60	×	60	−400
	60	7	60	−400
	60	10	60	−400
	60	15	60	−400
Schottky h^+ [2-5]	100	×	33	+900
	60	7	60	+900
	60	10	60	+900
	100	15	300	+900

5. Analyses & results

5.1. High voltage determination

In-situ measurements have been carried out at CPPM in order to ascertain the best bias value for each detector configuration. To this end, we used the 3 detectors mounted on the DE2 boards for which the output signal of the spy pixel was re-amplified at the exit of the OTA and then sent to a multi-channel analyzer (MCA-Spectrum Technics). 200 s exposures have been taken for different high voltage values. Except for the Ohmic type, which has been cooled down (due to high leakage current) at 23°C using running water, the measurements were done without any cooling system. Spectra being acquired with the same exposure time, their integrals represent pixel counts. Optimizing bias implies to maximizing signal amplitude while keeping peak resolution (FWHM) as small as possible.

Accidental failure of the DE2 board prevented analysis of the spectral response of the Schottky h^+ [2-1]. Results for both remaining assemblies are presented on Figure 5.

5.1.1. Ohmic e^-

In this case, increasing the bias value improves the peak resolution but one can also notice that the peak position is gradually shifted toward lower energies of the spectrum. This effect is attributed to the increase of the leakage current with the bias, which in turn tends to change the XPAD3.2 preamplifier gain as demonstrated by simulation. The optimal bias voltage would then be the one combining the best energy resolution together with a stable leakage current. According to this, and even though this behavior is not intuitive at all, one can assess that the most relevant high voltage value for this configuration is −200 V (below this value, the leakage current becomes too unstable). After calibration, the calculated FWHM of the 59.5 keV pic at −200 V is 2.43 keV corresponding to a RMS of about 1.03 keV or 232 e^-.

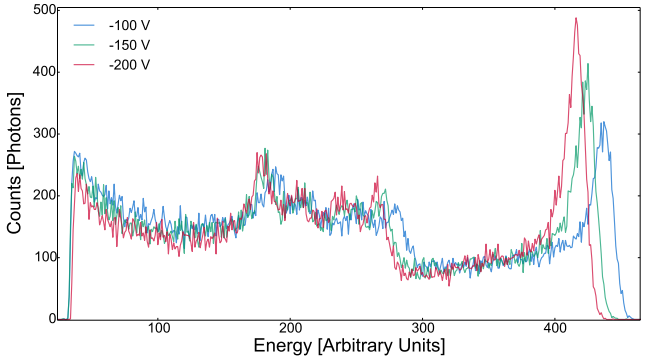

(a) Ohmic e^- [1-1]

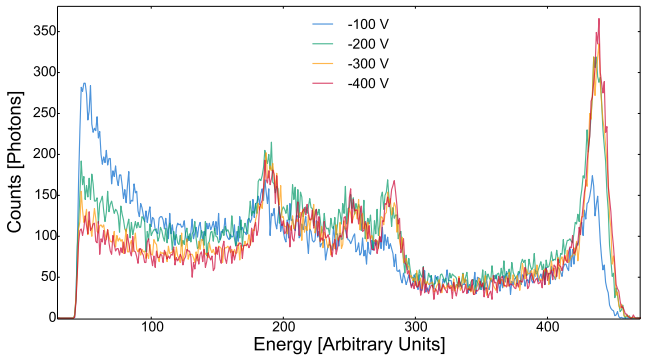

(b) Schottky e^- [3-5]

Figure 5: Americium spectra from a multi-channel analyzer with respect to different bias values for both Ohmic e^- and Schottky h^+ detector configurations.

5.1.2. Schottky e^-

The efficiency of the Schottky type in electrons collection mode appears to be stable above 200 V (in absolute value), so is the pic position at 59.5 keV, which remains in between channels 435 and 439 of the spectrometer (*cf.* Figure 5b). Below −400 V the leakage current becomes stronger and unstable, nevertheless it does not seem to be a problem as neither the efficiency nor the resolution are varying under −200 V. Therefore it seems then reasonable to set the optimized bias value to −400 V for this configuration. After calibration, the calculated FWHM of the 59.5 keV pic is 2.3 keV corresponding to a RMS of about 0.94 keV or 213 e^-, which is far above the electronic noise (*cf.* Table 3).

5.1.3. Schottky h^+

Since we were not able to produce the spectra for the Schottky h^+ detector, we decided to use the optimized bias value of +900 V found by S. Basolo *et al.* [3] for their tests on a quasi-similar p-type CdTe based XPAD3.1 detector.

5.2. Calibrated images quality

At SOLEIL, using the 12 keV calibration maps performed on the *Métrologie* beamline, we produced 100 s exposure images at 24 keV for 3 detector configurations. The corresponding results are presented on Figure 6.

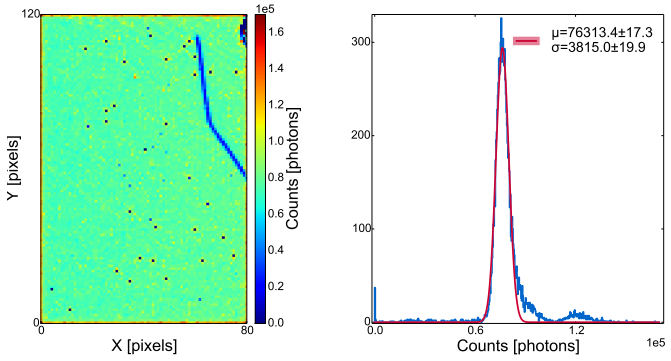

(a) Ohmic e^- [1-3]

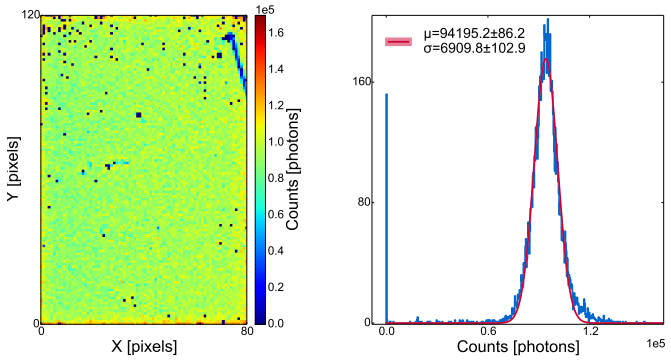

(b) Schottky e^- [3-2]

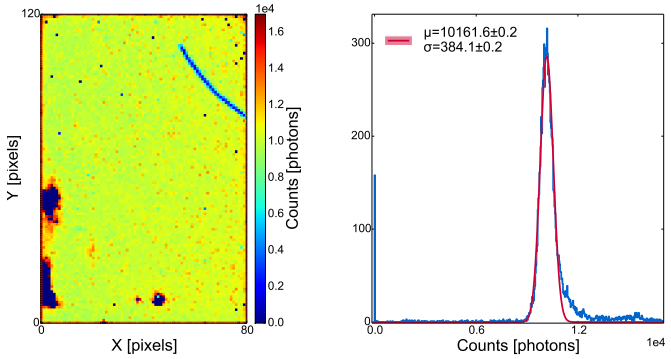

(c) Schottky h^+ [2-5]

Figure 6: 100 s exposure images of each detector tested at SOLEIL observed at 24 keV using a 12 keV (*i.e.* at half energy) *ad hoc* calibration. The efficiency loss noticeable for the Ohmic e^- and especially for the Schottky h^+ can be explained by the fact that their biases have not been optimized (+400 V instead of +900 V for the Schottky h^+ and −100 V instead of −200 V for the Ohmic e^-, *cf.* Table 4b and §4.2).

On all images, the high voltage wire on the sensor is clearly visible at the top right hand corner. It is also interesting to notice that the edge pixels are behaving differently (*i.e.* counting slightly more). This effect, which is probably due to insufficient guard ring charge collection, is responsible for the presence of a bump on the right side of the count distributions, especially on figures 6a and 6c.

Apart from 3 dead zones caused by the manipulation of the chip, the Schottky h^+ provides a detection surface of good quality with very few defective pixels. On the other hand the Schottky e^- sensor exhibits many unconnected/defective pixels, especially in his upper half. Finally, Ohmic e^- sensor presents sporadic small regions with non-optimally working pixels that are distributed all over the image. (see Figure 6a). If we look more closely at these regions (*cf.* the four enlarged areas displayed in Figure 7), we notice cross patterns around weak pixels. Reasons for this anomaly are not fully understood but seems related to a bad charge collection on the "central" pixel, which in turn leads to more charge collected by its four closest neighbours.

Excluding dead pixels from the analysis, we found that the dispersion of the counts was almost twice better in the case of Schottky h^+ chip (∼ 3.9 %) compared to Schottky e^-, and 30 % better in the case of Schottky h^+ compared to Ohmic e^-.

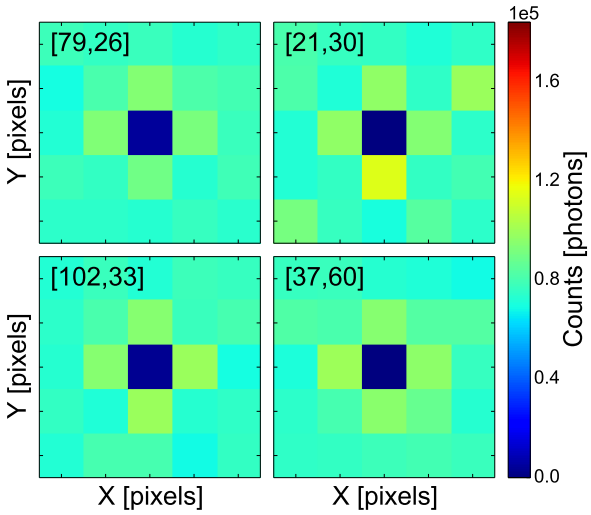

Figure 7: Typical examples of cross patterns due to unconnected bumps on the Ohmic e^- [1-3] sensor. The charge of the unconnected pixel is evenly shared between the closest neighbouring pixels.

Using non-optimized bias values for the Ohmic e^- and Schottky h^+ detectors is responsible for a loss of efficiency (almost a factor 10 loss for the Schottky h^+!) with respect to the Schottky e^- that appeared retrospectively to have been set to an optimized bias (see the mean values μ on Figure 6). The effect from the un-optimized biases can also be seen when looking at the pixel threshold as a function of the energy. Having access to a wide range of energy (from 8 to 40 keV) on the *Métrologie* beam line, we were able to assess the linearity of the detectors as a function of energy (*cf.* Figure 8).

We extracted the local threshold of each individual "S-curve" using the *ad hoc* method (*cf.* § 3.2) and computed their median and normalized median absolute deviation (nMAD) statistics for each energy (blue points and error bars on Figure 8). Finally, a χ^2 fit was performed for each tested configuration to assess for the significance of the linear relation of the DAC with respect to energy. The resulting p-values confirmed a perfect compatibility.

The chips being similar, we expected to have the same slope value for each configuration, but instead, we observed a slightly higher value for the Ohmic e^- and a much higher value for the

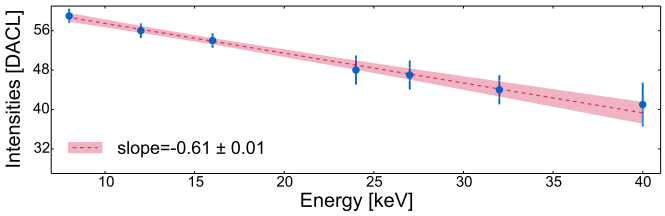

(a) Ohmic e⁻ [1-3]

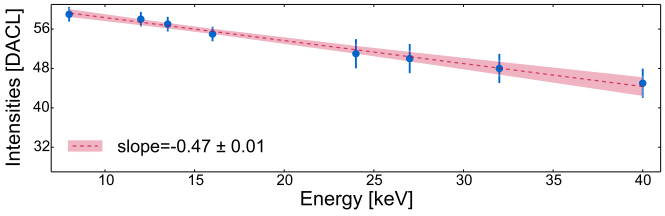

(b) Schottky e⁻ [3-2]

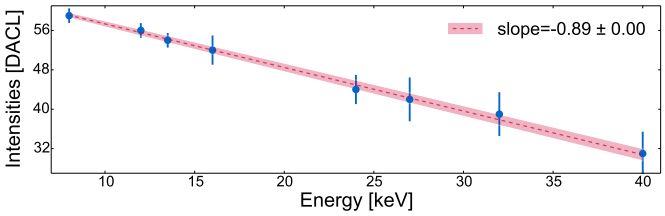

(c) Schottky h⁺ [2-5]

Figure 8: Median threshold value over the pixel matrix at each energy for all detector configurations. The error bar on each point represents the dispersion (normalized median absolute deviation) of the DACL at a given energy. A linear χ^2 adjustment is made to estimate the equivalence DAC / energy and its significance with a straight line.

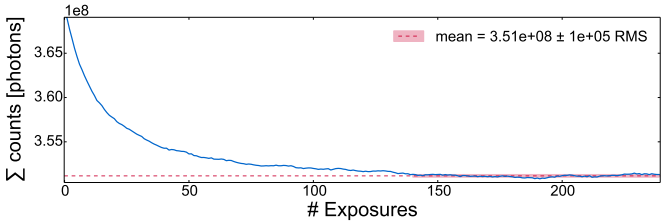

(a) Ohmic e⁻ [1-3] — No high voltage reset

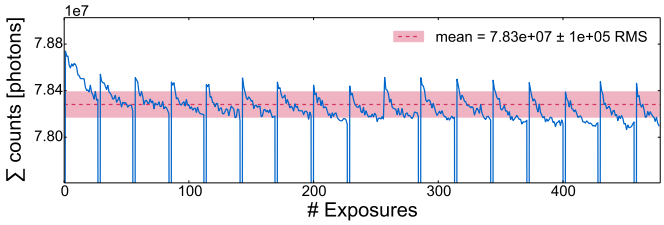

(b) Schottky e⁻ [3-5] — High voltage reset every 20 minutes

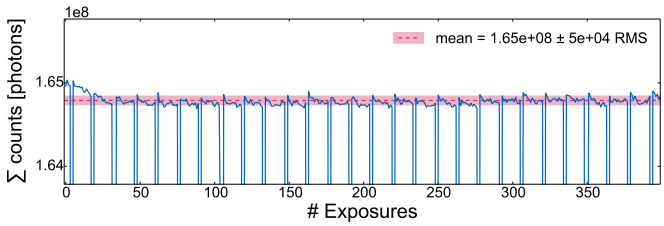

(c) Schottky h⁺ [2-4] — High voltage reset every 10 minutes

Figure 9: Counting stability of three XPAD detector configurations with respect to high voltage reset cycles (*cf.* Table 5).

Schottky h⁺ due to the non optimized biases.

5.3. *Stability*

The counting stability test consists in taking successive images and following the evolution over time of the integrated counts. However, due to the polarization effects in CdTe with Schottky contacts [21], the exposures have to be interspersed with bias resets after a certain amount of time. This effect is attributed to the trapping of electrons in deep acceptor levels [22, 23], which tends to decrease progressively the amplitudes of the pulses with time. Decreasing the bias value to zero and raising it again to the working value restores the former amplitude, as was observed in [3]. Results of the tests performed at CPPM and ESRF are shown on figures 9 and 10, respectively. As ESRF is not operating in the "top-up" mode to compensate for electron losses in the storage ring, we can notice a slow decline of the counting rate over the duration of the experiment (a refilling of the beam is visible on Figure 10f).

5.3.1. *Measurements at* CPPM

In the case of the Ohmic configuration stability as measured at CPPM, no polarization was expected, so we simply took successive 150 s exposures without any bias resets. The counting variation, as seen in Figure 9a, shows a slow counting decrease of about 5% before stabilization around exposure # 140 (*i.e.* after more than 5 hours).

The average stability of the Schottky e⁻ configuration over time shows a regular decreasing pattern of 1.3 ‰ RMS in between reset cycles (*cf.* figures 9b). For the Schottky h⁺ average stability on the other hand (*cf.* 9c), the pattern is present but less obvious, probably because the reset cycles are shorter (10 min instead of 20 minutes for the Schottky e⁻). Nevertheless, even by taking into account the time difference between the cycles, the variation in this case is distinctly smaller (about 0.6 ‰ RMS).

Direct comparison of the measurements conducted at CPPM shows that the counting rate of the Schottky h⁺ configuration is the most stable one and that both the Schottky h⁺ and e⁻ detectors are much more stable than the Ohmic one (when resets are applied). However, it is interesting to note that in its stable region (exposures 140 to 240), the Ohmic detector shows a dispersion of 0.2 ‰ RMS (*cf.* 9a).

5.3.2. *Measurements at* ESRF

To corroborate our stability analysis performed at CPPM, we selected a new couple of Schottky assemblies of each kind (electrons collection mode [3-4] and holes collection mode [2-5]) and repeated the operation on the D2AM beam line using this time the optimized biases (*cf.* §5.1) and the *ad hoc* calibration. The characteristics of the measurements are presented in

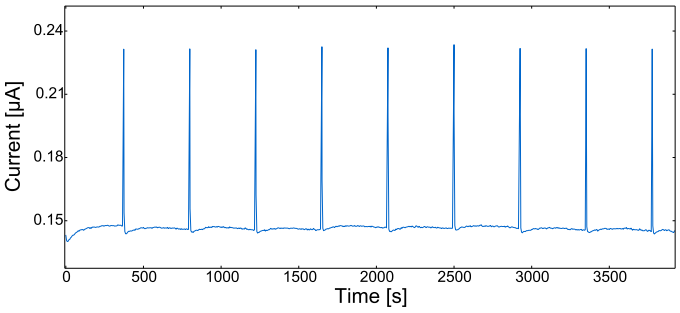

(a) High voltage reset every 7 minutes

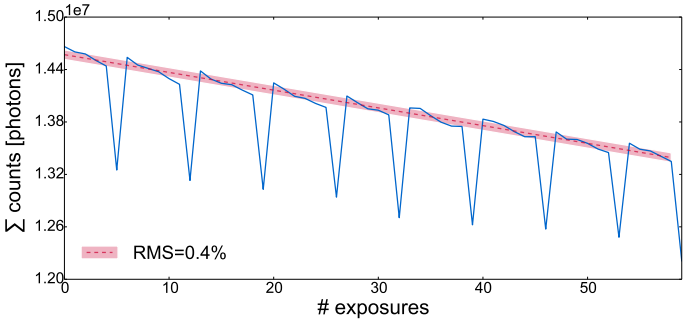

(b) High voltage reset every 7 minutes

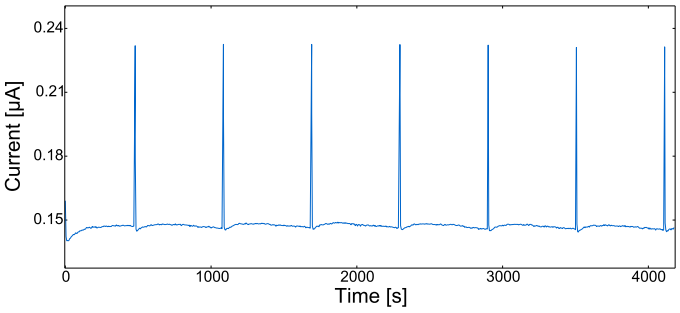

(c) High voltage reset every 10 minutes

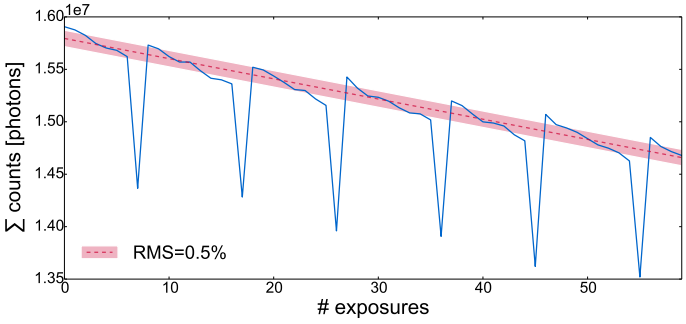

(d) High voltage reset every 10 minutes

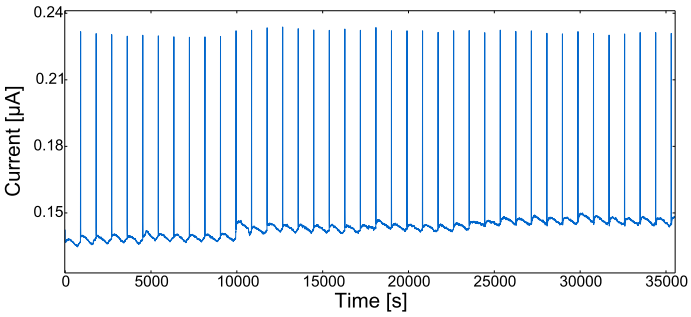

(e) High voltage reset every 15 minutes

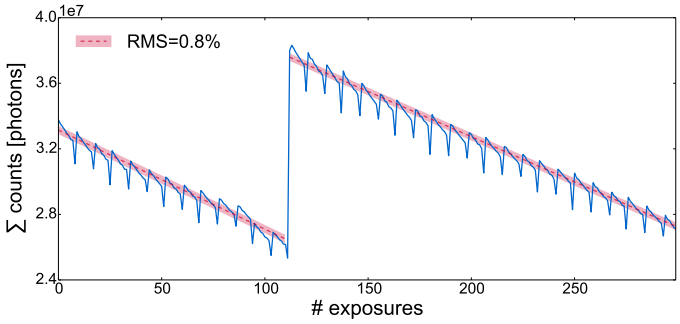

(f) High voltage reset every 15 minutes

Figure 10: Leakage current and counting stability of the XPAD detector in Schottky holes collection mode (Schottky h^+ [2-5]) with respect to different high voltage reset cycles. (*cf.* Table 6)

Table 6 and the measurements themselves are shown on Figure 10 for the Schottky h^+.

Except for the slow decrease due to the electron losses in the storage ring, and even though we cannot compare directly the values, the counting behavior over time of the Schottky h^+ configuration displayed on Figure 10d is compatible with what was observed at CPPM: a regular fast decreasing pattern in between reset cycles. As for the evolution for the different reset cycles, the RMS increases logically from 7 minutes to 15 minutes long cycles (from 0.4 % to 0.8 %) which might be negligible in most cases. Note that the factor 10 stability difference (in RMS percentage) between tests at ESRF and CPPM comes from the fact that the detector [2-4] is intrinsically more stable than the detector [2-5].

On the other hand, the counting behavior over time of the Schottky e^- [3-4] configuration was rather different and more chaotic than what we expected according to our prior results and yet not understood.

5.4. *Homogeneity — pixels discrepancies*

During our stability tests, we noticed that some pixels (approximately one third) were behaving differently than the counts integral behavior over the full matrix. Figure 11 shows four pixels illustrating the possible behaviors in between resets from decreasing to increasing via stability.

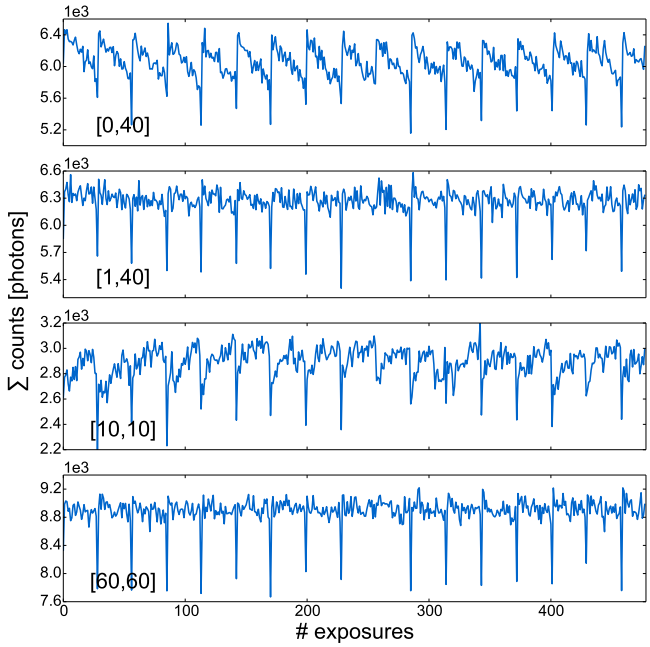

Figure 11: Discrepancies of four pixels from the Schottky e^- [3-5] detector configuration. The differences of the count rate evolutions in between resets are clearly visible from one pixel to an other

In order to have a more accurate representation of these behaviors, we took into account a group of acquisitions between two resets. The ohmic stability measurements needing no resets, we simply considered a large zone on the stable plateau (*i.e.* after 5 hours). For each pixel, we computed the average count of the 5 firsts and 5 lasts exposures among these acquisitions. We then proceeded to the difference of these two values for the entire pixel matrix. The histogram and spatial distribution of these differences are represented on Figure 12 for three of the detector configurations tested at CPPM.

One can notice that each histogram is centered close to 0 as one could expect. However, the RMS of the distributions is too large with respect to a Poissonian statistics. Indeed, with an average count rate of 10000 counts / acquisition, one might expect for a Poissonian statistics an RMS of $\frac{\sqrt{10000}}{\sqrt{10}} = 31.6$. We also observed that the edge pixels tend to decrease during an acquisition. For pixels in the center, the situation is different and some line shaped structures of increasing patterns appear distinctly on each sensor. On the other hand, around unconnected pixels, the same decreasing pattern as for edge pixels is visible. In between linear structures, pixel behaviours seem rather stable and homogeneous.

The Schottky h^+ and Ohmic e^- configurations are less affected by these structures than the Schottky e^-, whose pattern looks like a piece of shattered glass (*cf.* Figure 12b). Although a single large negative band is visible in the middle of the Schottky h^+ and weak positive stripes are scattered all around the lower half of the Ohmic e^-. It is also important to note that the RMS of the Schottky h^+ histogram is almost half the value of Ohmic e^- one making its structures less marked. Note that these lines could come from crystal dislocations and would then be independent of the detector types. Obviously, we will need more hybrids to confirm this hypothesis.

Changing the bias value or the intervals do not remove the structures but a different bias slightly changes the structures intensity. Switching between different acquisition cards does not sort out the problem either.

6. Discussion

The first impression when looking at the various data gathered for the presented analyses is that the CdTe hybrid production is widely heterogeneous. One of the tested detector was even unusable from the start, most of its pixels being unconnected. The obvious non-uniformity between the hybrid samples of a same kind makes the selection process for the construction difficult.

Nevertheless, when putting aside the "bad" areas, our tests on the image quality of 3 hybrids at 24 keV after *ad hoc* calibration are promising, especially for the Schottky h^+ for which we measured a dispersion smaller than 4 % (*cf.* § 5.2), although its efficiency was affected by a too low bias setting.

The tests on the average counting stability with time show that by applying regular reset cycles, both Schottky configurations are much more stable than the Ohmic one in the short-term (the Ohmic detector needs more than 5 hours to be stable, incidentally losing 5 % efficiency). Note that there is no point at applying bias resets to the Ohmic configuration seeing as the leakage current of the Ohmic being much higher than for the Schottky configuration, its only interest is that it does not require bias resets. The chosen reset cycle for the Schottky will

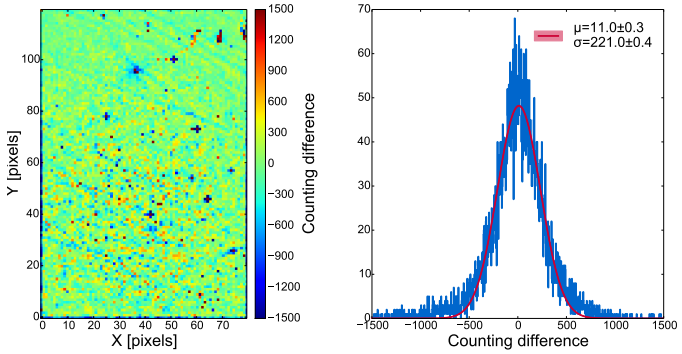

(a) Ohmic e⁻ [2-3]

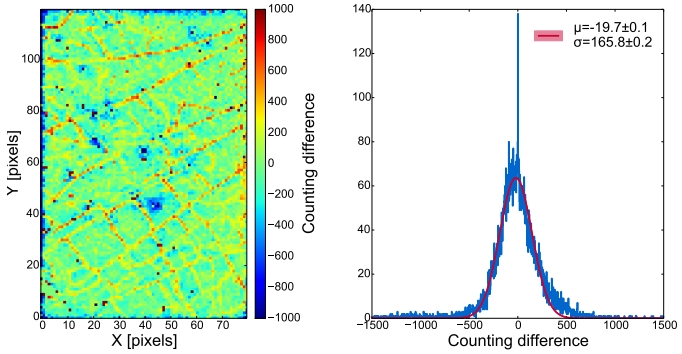

(b) Schottky e⁻ [3-5]

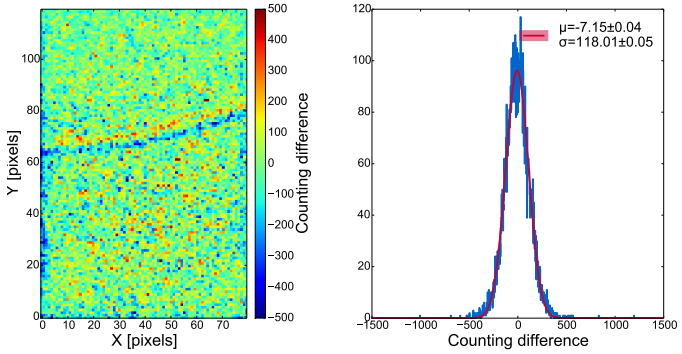

(c) Schottky h⁺ [2-4]

Figure 12: Histograms and spatial distributions of the pixel evolutions during an acquisition. The data represent the difference between the average count rate of the 5 firsts and 5 lasts exposures among the acquisitions in between resets.

depend on the ongoing experiments, but we observed on a synchrotron beam line that cycles of less that 15 minutes lead to RMS < 1 % for the Schottky h⁺ (*cf.* Figure 10e).

The homogeneity analysis of paragraph §5.4, shows that the behavior (increasing or decreasing counting with time) of the pixels varies across the matrix. Especially, the pixels neighbouring an unconnected zone seem to have a strong decreasing counting pattern, so are the edge pixels, despite the presence of a guard ring. Therefore, it is not reasonable to rely on the single spy-pixel to assess the full detector matrix. This phenomenon leads to a heterogeneity of the pixel counting stability with time. That being said, the Schottky e⁻ configurations that we tested seems to be more affected than the others (its structures are more pronounced). The structures intensity seems to depend on the applied bias, at least for the Schottky h⁺. All in all, even if these structures are worrying, we saw that the overall fluctuation for Schottky h⁺ is smaller than 1 %.

All hybrid types show a very good DAC linearity in function of energy (p-value of 1) with an error on the slope between 1 and 2 % according to the configuration (*cf.* Figure 8). Although, the error bars get bigger at higher energy.

Finally, the energy resolution seems to be pretty much the same between Schottky e⁻ and Ohmic e⁻ according to the spectra measured in §5.1, even though the Schottky types have supposedly a better spectral resolution.

7. Conclusions

This article presented a preliminary study on 3 samples of 3 hybrids (Ohmic e⁻, Schottky e⁻ and Schottky h⁺) provided by Acrorad for the sensors and Ajat for the hybridization. It aimed at smoothing the rough edges off for the selection of the best hybrid in order to build a large area detector for hard X-ray.

Our first conclusion is that, due to the important discrepancies in between hybrids of a same type, more statistics for each detector are needed to achieve a proper decision. Although, in the light of these preliminary results, and according to previous studies [3], the Schottky e⁻ type detectors, which seems less robust, will be discarded from further testing. We will then focus on studying the Ohmic e⁻ and Schottky h⁺ detector configurations.

Nonetheless, in the light of the homogeneity and image quality tests, and in absence of further statistics, the Schottky in holes collection mode appears to be the most reasonable choice for the moment.

Acknowledgment

This work was supported by the ITMO Cancer within the Plan Cancer 2009-2013 under Grant N° PC201235 and the European project Calipso, Grant agreement N° 312284. The authors are also indebted and grateful to the CRG-BM02-D2AM and *Métrologie* beamlines at ESRF and SOLEIL, respectively.

References

[1] K. H. Becks, P. Borghi, J. M. Brunet, M. Caccia, J. C. Clemens, M. Cohen-Solal, B. Courty, W. de Boer, P. Delpierre, J. Drees, P. Gerlach, K. W. Glitza, I. M. Gregor, L. Guglielmi, F. Hartmann, J. M. Heuser, J. J. Jaeger, M. Kaiser, S. Kersten, D. Knoblauch, A. Koepert, H. Leb, F. Ledroit, G. Maehlum, C. Meroni, S. Meyer, K. Moenig, T. Mouthuy, H. Pert, M. Pindo, M. Raymond, N. Redaelli, L. Roos, D. Sauvage, P. Sicho, G. Tristram, J. P. Turlot, B. Uberschar, G. Vegni, V. Vrba, M. Wielers, The DELPHI pixels, Nuclear Instruments and Methods in Physics Research Section A 386 (1997) 11–17.

[2] J. F. Bérar, L. Blanquart, N. Boudet, A pixel detector with large dynamic range for high photon counting rates, Journal of Applied Cristallography (2002).

[3] S. Basolo, J. F. Bérar, N. Boudet, P. Breugnon, B. Chantepie, J. C. Clemens, P. Delpierre, B. Dinkespiler, S. Hustache, K. Medjoubi, M. Menouni, C. Morel, P. Pangaud, E. Vigeolas, A 20 kpixels CdTe photon-counting imager using XPAD chip, Nuclear Instruments and Methods in Physics Research Section A 589 (2008) 268–274.

[4] R. Ballabriga, M. Campbell, E. Heijne, X. Llopart, L. Tlustos, W. Wong, Medipix3: A 64k pixel detector readout chip working in single photon counting mode with improved spectrometric performance, Nuclear Instruments and Methods in Physics Research Section A: Accelerators, Spectrometers, Detectors and Associated Equipment 633 (2011) S15–S18.

[5] P. Pangaud, S. Basolo, N. Boudet, J.-F. Berar, B. Chantepie, P. Delpierre, B. Dinkespiler, S. Hustache, M. Menouni, C. Morel, XPAD3: A new photon counting chip for X-ray CT-scanner, Nuclear Instruments and Methods in Physics Research Section A: Accelerators, Spectrometers, Detectors and Associated Equipment 571 (2007) 321–324.

[6] B. Henrich, A. Bergamaschi, C. Broennimann, R. Dinapoli, E. F. Eikenberry, I. Johnson, M. Kobas, P. Kraft, A. Mozzanica, B. Schmitt, PILATUS: A single photon counting pixel detector for X-ray applications, Nuclear Instruments and Methods in Physics Research Section A 607 (2009) 247–249.

[7] J. F. Bérar, N. Boudet, P. Breugnon, B. Caillot, B. Chantepie, J. C. Clemens, P. Delpierre, B. Dinkespiller, S. Godiot, C. Meessen, M. Menouni, C. Morel, P. Pangaud, E. Vigeolas, S. Hustache, K. Medjoubi, XPAD3 hybrid pixel detector applications, Nuclear Instruments and Methods in Physics Research Section A 607 (2009) 233–235.

[8] F. Cassol Brunner, J. C. Clemens, C. Hemmer, C. Morel, Imaging performance of the hybrid pixel detectors XPAD3-S, Physics in Medicine and Biology 54 (2009) 1773–1789.

[9] K. Medjoubi, S. Hustache, F. Picca, J. F. Bérar, N. Boudet, F. Bompard, P. Breugnon, J. C. Clemens, A. Dawiec, P. Delpierre, B. Dinkespiler, S. Godiot, J. P. Logier, M. Menouni, C. Morel, M. Nicolas, P. Pangaud, E. Vigeolas, Performance and Applications of the CdTe- and Si-XPAD3 photon counting 2D detector, Journal of Instrumentation 6 (2011) C01080.

[10] K. Medjoubi, A. Thompson, J.-F. Berar, J.-C. Clemens, P. Delpierre, P. Da Silva, B. Dinkespiler, R. Fourme, P. Gourhant, B. Guimaraes, S. Hustache, M. Idir, J.-P. Itié, P. Legrand, C. Menneglier, P. Mercere, F. Picca, J.-P. Samama, Energy resolution of the CdTe-XPAD detector: calibration and potential for Laue diffraction measurements on protein crystals, Journal of Synchrotron Radiation 19 (2012) 323–331.

[11] F. Cassol Brunner, M. Dupont, C. Meessen, Y. Boursier, H. Ouamara, A. Bonissent, C. Kronland-Martinet, J. Clemens, F. Debarbieux, C. Morel, First K-Edge Imaging With a Micro-CT Based on the XPAD3 Hybrid Pixel Detector, Nuclear Science, IEEE Transactions on 60 (2013) 103–108.

[12] J. Singh, Electronic and Optoelectronic Properties of Semiconductor Structures (2003).

[13] M. Funaki, Y. Ando, R. Jinnai, A. Tachibana, Development of CdTe detectors in Acrorad, Internal publication (2007).

[14] R. O. Bell, G. Entine, H. B. Serreze, Time-dependent polarization of CdTe gamma-ray detectors, Nuclear Instruments and Methods 117 (1974) 267–271.

[15] H. L. Malm, M. Martini, Polarization Phenomena in CdTe Nuclear Radiation Detectors, Nuclear Science, IEEE Transactions on 21 (1974) 322–330.

[16] P. Pangaud, S. Basolo, N. Boudet, J.-F. Berar, B. Chantepie, J.-C. Clemens, P. Delpierre, B. Dinkespiler, K. Medjoubi, S. Hustache, M. Menouni, C. Morel, XPAD3-S: A fast hybrid pixel readout chip for X-ray synchrotron facilities, Nuclear Instruments and Methods in Physics Research Section A: Accelerators, Spectrometers, Detectors and Associated Equipment 591 (2008) 159–162.

[17] A. Dawiec, Development of an ultra-fast X-ray camera using hybrid pixel detectors, PhD thesis (2011) 1–181.

[18] C. Buton et al., Calibration of the XPAD3.2 hybrid-pixels quantum X-ray detector (in preparation), Journal of Synchrotron Radiation (2014).

[19] C. Ponchut, Correction of the charge sharing in photon-counting pixel detector data, Nuclear Instruments and Methods in Physics Research Section A 591 (2008) 311–313.

[20] F. Cassol Brunner, D. Benoit, J. F. Bérar, J. C. Clemens, C. Morel, Study of the charge sharing effect in the photon-counting pixel detector XPAD3-S, Nuclear Instruments and Methods in Physics Research Section A 633 (2011) 111.

[21] M. Niraula, A. Nakamura, T. Aoki, Y. Tomita, Y. Hatanaka, Stability issues of high-energy resolution diode type CdTe nuclear radiation detectors in a long-term operation, Nuclear Instruments and Methods in Physics Research Section A 491 (2002) 168–175.

[22] H. Toyama, A. Higa, M. Yamazato, T. Maehama, R. Ohno, M. Toguchi, Quantitative Analysis of Polarization Phenomena in CdTe Radiation Detectors, Japanese Journal of Applied Physics 45 (2006) 8842–8847.

[23] A. Cola, I. Farella, A. M. Mancini, A. Donati, Electric Field Properties of CdTe Nuclear Detectors, IEEE Transactions on Nuclear Science 54 (2007) 868–872.